Nuclear Science and Techniques (2026) 37:31
https://doi.org/10.1007/s41365-025-01834-w

Insights into the helium bubbles coarsening behavior in the post-irradiated annealing 304L stainless steel processed by laser powder bed fusion

Si-Yi Qiu[1] · **Yan-Lin Gu**[1] · **Yu-Yu Guo**[1] · **Hui Liu**[2] · **Lei Huang**[3] · **Ai-Jun Huang**[4] · **Juan Hou**[1,5]

Received: 3 April 2024 / Revised: 21 June 2024 / Accepted: 19 August 2024 / Published online: 4 January 2026

Abstract

350 keV He^+ ions were injected into laser powder bed fusion (LPBF)-processed 304L stainless steel and traditional rolled 304L stainless steel with a flux of 1×10^{17} ions/cm^2 at room temperature, followed by annealing at 750 °C for 10, 100, and 300 h, respectively. The results showed that material swelling due to helium bubble coarsening was almost not observed in either the LPBF or rolled samples after 10 h of annealing duration. Rapid coarsening and swelling of bubbles occurred in the rolled samples, but only moderate bubble growth occurred in the LPBF sample after annealing for 100 h. After annealing for 300 h, the helium bubbles in both samples tended to grow steadily. For 10 h of annealing, the irradiated samples were in a disequilibrium state, and the apparent activation energy (E^{act}) calculated by the Arrhenius model determined that helium atoms tended to diffuse through the displacement mechanism, and helium bubbles grew under the migration and coalescence (MC) mechanism. With annealing times over 100 h, the high-density dislocations and nano-oxide particles in the LPBF sample still had a strong trapping effect on the movement and growth of helium bubbles. After annealing for 300 h, the cellular subgrains in the LPBF sample decomposed, and the nano-oxide particles had no trapping effect on the helium bubbles. At this time, the dislocation structure played a primary role in suppressing the growth of helium bubbles, and the radiation resistance of the LPBF sample remained superior to that of the rolled samples.

Keywords Helium atom diffusion · Helium bubble growth · Selective laser melting of stainless steel · Annealing time · Local microstructure

1 Introduction

Laser powder bed fusion (LPBF) technology is one of the most fastest growing technologies in metal additive manufacturing, which can produce critical stainless steel components for reactor in cores with complex shapes, helping to achieve integrated manufacturing and rapid prototyping, providing new options and opportunities to overcome the bottleneck of traditional processing technology. Therefore, it has attracted widespread attention in the field of nuclear power plants [1, 2]. Austenitic stainless steel is used as the key structural material for reactor core components owing to its excellent high-temperature mechanical and corrosion resistance properties [3]. Furthermore, the service environment involves high-flux and long-term neutron irradiation and is susceptible to (n, a) transmutation reactions with the material, which inevitably produce an abundance of helium atoms in the structural material. Helium is an inert element

---

This work was supported by the National Natural Science Foundation of China (Nos. U22B2067 and 52073176).

✉ Juan Hou
hou18217727686@163.com

[1] School of Materials and Chemistry, University of Shanghai for Science and Technology, Shanghai 200093, China

[2] Shanghai Institute of Applied Physics, Chinese Academy of Sciences, Shanghai 201800, China

[3] Suzhou Becreative-AM Co. LTD, Suzhou 215000, China

[4] Monash Centre for Additive Manufacturing (MCAM), Notting Hill, VIC 3168, Australia

[5] State Key Laboratory of Nuclear Power Safety Monitoring Technology and Equipment, Shenzhen 518172, China

that does not combine with other atoms or dissolve in the material matrix. As the concentration of helium atoms continues to accumulate and precipitate, helium vacancy clusters are formed and ultimately agglomerate into helium bubbles [4, 5]. Helium bubbles are prone to aggregation and coarsening at grain boundaries, phase boundaries, and dislocations, which seriously alters the microstructure of the material and leads to surface foaming [6], expansion [7, 8], and helium embrittlement [9, 10], reducing the mechanical properties of the material and seriously affecting the safety and economy of nuclear power plants.

It is widely known that nanoscale ultrafine structure possesses high-volume fraction interfaces, including grain boundaries, phase boundaries, and layer interfaces, which can serve as defect sinks to improve radiation resistance [11]. Zinkle et al. [12] also demonstrated that nanocrystalline materials, oxide dispersion strengthened (ODS) steel, and nanostructured ferrite alloys exhibit high defect sinking strength $\left(> 10^{16}/\text{m}^2\right)$, effectively suppressing the radiation-induced material hardening. Numerous studies have indicated [4, 13, 14] that the overall growth of helium bubbles is ultimately inhibited in materials by introducing high-density defect sinks (such as grain boundaries, oxide particles, and dislocations) to capture helium atoms and impede the migration and coalescence of helium bubbles. It is now widely accepted that LPBF-processed stainless steel possesses unique microstructural characteristics, including ultrafine cellular subgrains, precipitates, and nano-oxide inclusions [15–19], which are of great significance for improving radiation resistance. Current research primarily focuses on the nucleation behavior of helium bubbles [20], whereas studies on the growth behavior of helium bubbles in LPBF stainless steels remain scarce [21]. Post-irradiation annealing (PIA) is the most commonly used method in laboratory research to gain insight into the behavior and controlling mechanisms of helium bubble growth, which is proven to be strongly dependent on the test conditions of annealing temperature and soaking time, and the material microstructure [4, 22]. Two main mechanisms involved in the coarsening of helium bubbles have been established based on numerous experimental and computational studies: (a) bubble migration and coalescence (MC) and (b) Ostwald ripening (OR) [21, 23–25]. At present, research on the evolution of helium bubbles with annealing temperature [23–26] and annealing time [27–30] has been relatively mature. P.D. Edmondson [31] irradiated a 14YWT nanostructured ferrite alloy with 335 keV He^+, followed by 10 and 100 h of heat treatment at 750°C. The results indicated that the distribution of helium bubbles became more inhomogeneous during heat treatment process, which may be related to grain orientation. Hui Liu [32] annealed LPBF-processed 304L stainless steel after helium ion implantation and proved that the LPBF 304L samples exhibited better radiation resistance compared to rolled counterpart when annealed at 600°C for 1 h. The controlling mechanism for bubble coarsening was assumed to be the MC mechanism. The limited research has primarily focused on the annealing temperature, while the evolution of bubbles with soaking time and the fundamental controlling mechanism in LPBF-processed stainless steel have not been investigated.

Therefore, it is necessary to elucidate the dependence of helium bubbles on annealing time and the evolution of the microstructure of LPBF-processed stainless steels. In this study, 350 keV He^+ ions were injected into LPBF 304L stainless steel and conventionally rolled 304L stainless steel samples at a flux of 1×10^{17} ions/cm^2 at room temperature and annealed at 750°C for 10, 100, and 300 h, respectively. The coarsening behavior of the helium bubbles in the LPBF and rolled samples was compared. Cross-section TEM (transmission electron microscopy) analysis showed that the LPBF sample exhibited superior resistance to helium bubble growth.

2 Experiment

2.1 Sample preparation

The 304L stainless steel LPBF samples in this study were manufactured using an EOS M280 machine in an argon gas atmosphere. Gas-atomized powder with a particle size ranging from 10 to 53 μm was utilized as the feedstock powder, and the printing parameters and chemical composition have been described in previous publications [20]. The LPBF and rolled sample (cut from a commercial 304L plate rolled at room temperature) were sectioned into small sample dimensions of 2 mm × 5 mm × 1 mm using wire-cutting techniques. The sample was gradually ground with 220–3000 grit sandpaper and polished with Al_2O_3 polishing solution to obtain a scratch-free sample. To remove residual stress on the surface, electrolytic polishing was carried out using 10% perchloric acid –90% ethanol at a voltage of 30 V and polishing for 15 s. The surface of the sample was sequentially cleaned using an ultrasonic cleaning instrument with acetone, alcohol, and deionized water. Finally, the sample was dried for subsequent irradiation experiments.

2.2 Helium ion implantation and annealing

The surfaces of the samples were mirror-polished, irradiated with raster beams, and then implanted with 350 keV helium ions at room temperature with a fluence of 1×10^{17} ions$/\text{cm}^2$ at the Institute of Semiconductors, Chinese Academy of Science. Details of the implantation test are provided in a previous publication [33]. Helium ion irradiation damage and He concentration profiles were calculated using SRIM (the Stopping and Range of Ions in Matter) [34] and are shown in Fig. 1. The peak ion concentration was approximately

0.8–0.9 µm away from the sample surface. The highest concentration of He was approximately 5.6 at%, and the maximum damage depth was approximately 1 µm beneath the surface. The samples were then annealed for 10, 100, and 300 h in a tube furnace at 700°C to gain insight into the helium bubble growth behavior, which were called as PIAed samples. The LPBF and rolled samples for TEM observation were prepared using a focused ion beam (FIB, FEI Nanolab 600) system to characterize the helium bubble density and distribution in the two states of as-irradiation and PIA. To ensure the accuracy of the experimental data, each sample was taken from the same sample within the peak damage zone, and the size and quantity of helium bubbles were measured using image software through several TEM images. The thickness of the TEM samples was determined using convergent beam electron diffraction (CBED). The samples were labeled as T1 (Rolled, implanted), T2 (Rolled, implanted + PIA at 700 °C for 10 h), T3 (Rolled, implanted + PIA at 700°C for 100 h), T4 (Rolled, implanted + PIA at 700 °C for 300 h); A1 (LPBF, implanted), A2 (LPBF, implanted + PIA at 700 °C for 10 h), A3 (LPBF, implanted + PIA at 700 °C for 100 h), A4 (LPBF, implanted + PIA at 700 °C for 300 h). TEM lamella thinness and experimental conditions are listed in Table 1.

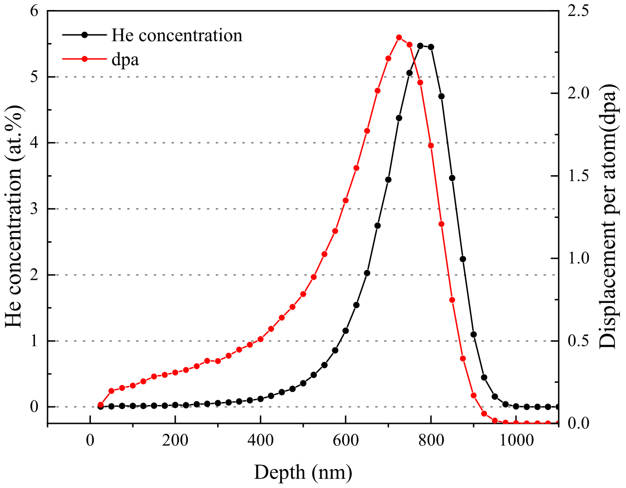

Fig. 1 Damage dose (red line) and He^+ ion implantation profile (black line) calculated by SRIM after irradiated by 350 keV He^+ ion to 1×10^{17} ion/cm^2 in the LPBF304L stainless steels

3 Results

3.1 The stability of the microstructure in laser powder bed fusion samples

LPBF 304L stainless steel generally exhibits finer grain sizes owing to the rapid solidification rates during the LPBF

Table 1 Marking of irradiated and post-irradiation annealed stainless steel samples

Label	Sample status	Sample thickness (nm)
T1	Rolled, implanted	52
T2	Rolled, implanted, PIA at 700 °C for 10 h	50
T3	Rolled, implanted, PIA at 700 °C for 100 h	50
T4	Rolled, implanted, PIA at 700 °C for 300 h	65
A1	LPBF, implanted	52
A2	LPBF, implanted, PIA at 700 °C for 10 h	50
A3	LPBF, implanted, PIA at 700 °C for 100 h	50
A4	LPBF, implanted, PIA at 700 °C for 300 h	65

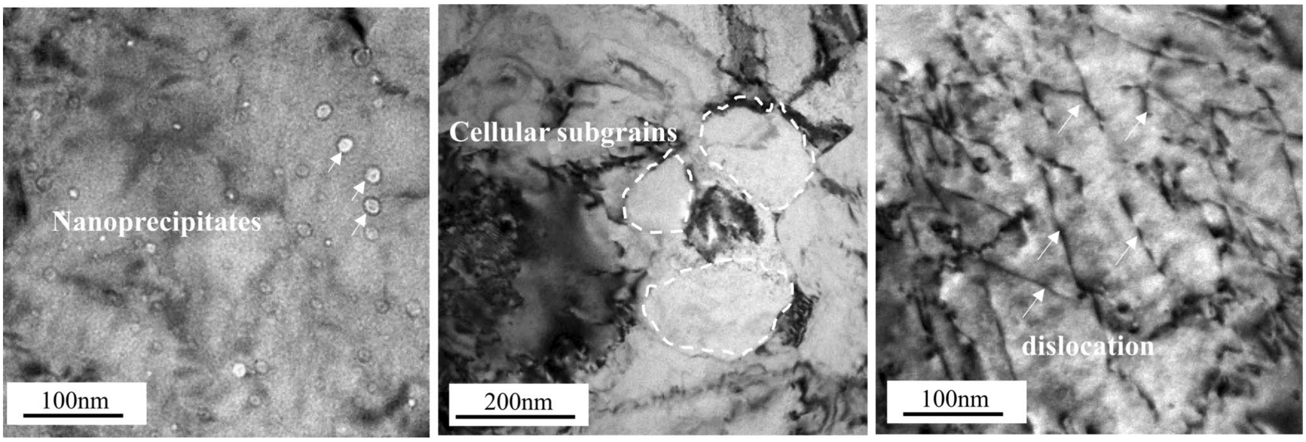

Fig. 2 TEM schematic diagram of the microstructure of no irradiated LPBF sample

process. The grain size of LPBF 304L stainless steel can range from approximately 1 to 10 µm [35], depending on the laser parameters and scan strategy used [36]. The grain size of stainless steel prepared using traditional processes typically ranges from 10 to 30 µm after recrystallization and annealing processes [37]. In the LPBF process, cellular structures are more easily formed at a relatively high ratio of temperature gradient (*G*) to cooling rate (*R*). As shown in Fig. 2, a small amount of nano-oxide particles, cellular subgrains, and linear dislocations were observed in the LPBF 304L stainless steel. In our previous study, we demonstrated that the cellular subgrains are composed of high-density dislocation walls [20]. As shown in Fig. 3, the cellular subgrains in the post-irradiation LPBF sample remained unaltered, indicating that irradiation had no significant influence on the cellular subgrain structure. This is consistent with the research findings of C. Fu. [19].

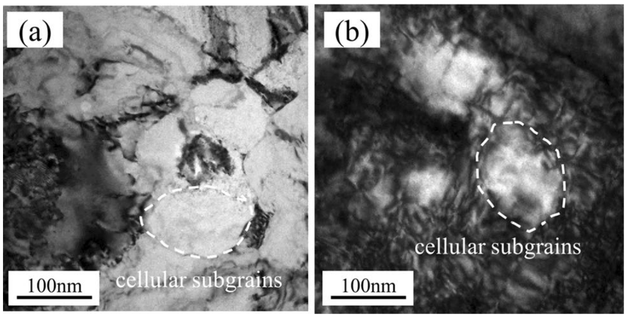

Fig. 3 TEM schematic diagram of the microstructure of LPBF sample: **a** no irradiated sample, **b** irradiated sample

In Fig. 4, the cellular subgrains of LPBF sample are still remained with the size range of approximately 0.5 µm even after annealing for 10 and 100 h, indicating that their structure remains relatively stable even after high-temperature annealing for 100 h. After annealing for 300 h, the cellular subgrains were decomposed, but many dislocations were still present.

3.2 Helium bubbles in the matrix

Figure 5 shows the distribution of helium bubbles in the two materials after He injection at room temperature. In the T1 rolled samples, the depth of the helium-causing damage

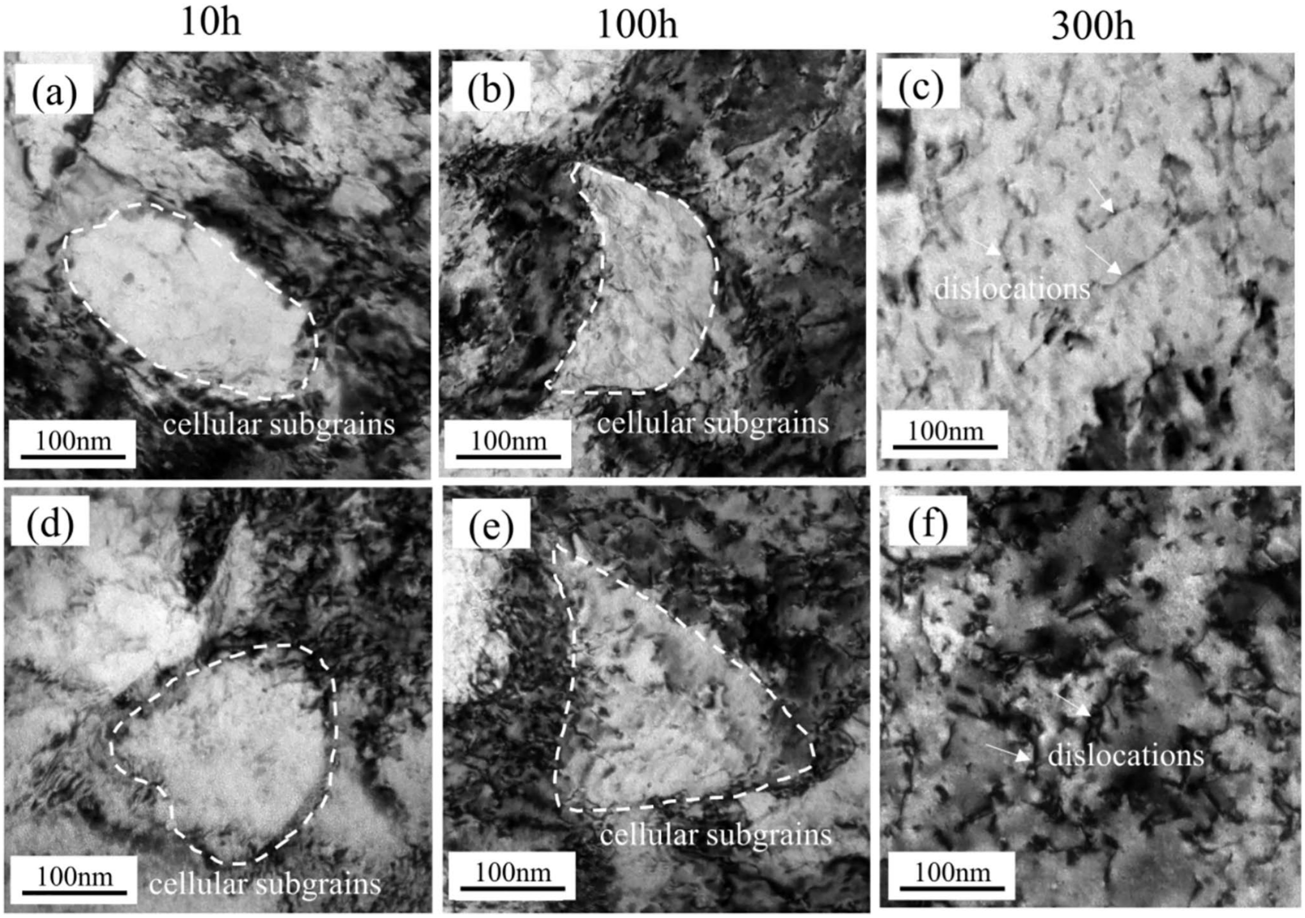

Fig. 4 TEM images of the microstructure of LPBF samples post-irradiation annealed at 700 °C for 10 h (**a**, **d**), 100 h (**b**, **e**), and 300 h (**c**, **f**)

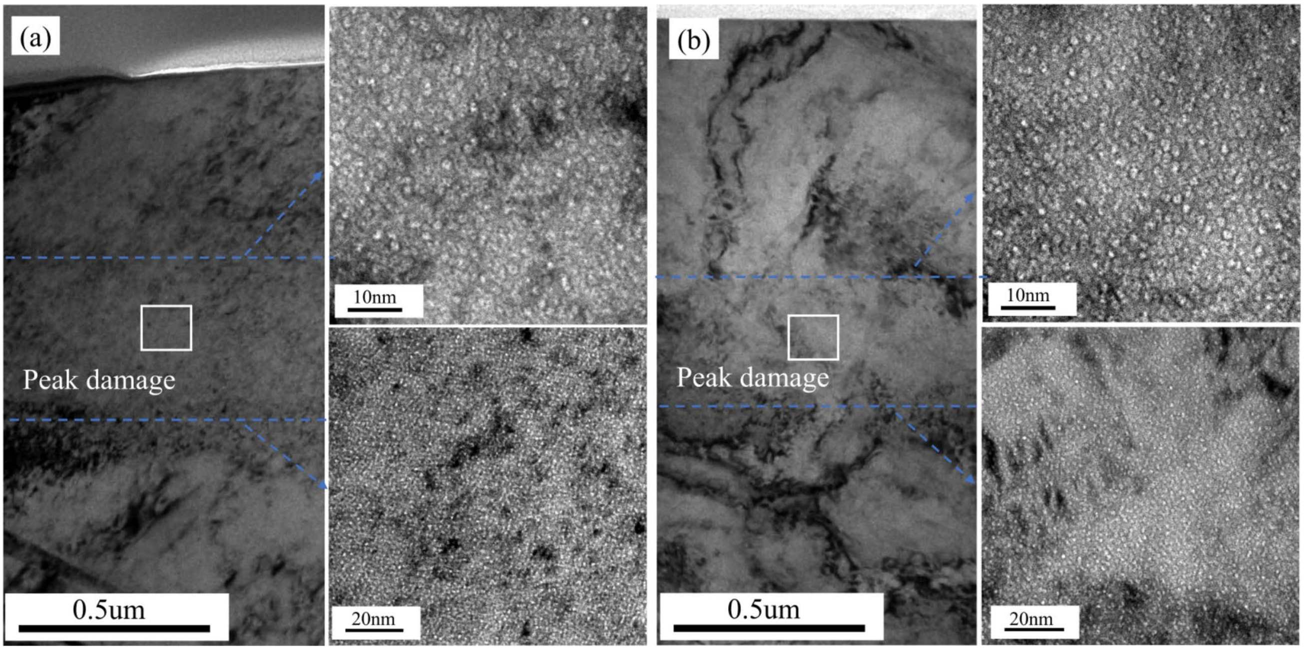

Fig. 5 TEM images of the **a** the rolled sample and **b** the LPBF sample after He$^+$ ion implantation in −500 nm under-focus condition

zone was approximately 980 nm, and the width was approximately 470 nm. The helium bubble size and density were 1.12 nm in diameter and 3.86×10^{24} m^{-3}, respectively. In the A1 LPBF samples, the depth of the helium bubble damage zone was approximately 950 nm, the width was approximately 430 nm, and the corresponding data were 1.0 nm in diameter and 1.12×10^{24} m^{-3} number density, respectively. This result demonstrates that the helium bubble nucleation and damage zone width in the LPBF sample are lower than those in rolled sample, which is consistent with our previous conclusion that the PLBF 304L stainless steel exhibits better irradiation resistance [20]. However, the helium bubble number density of both samples is one order of magnitude higher than that in the literature [20], caused by our higher helium injection dose.

As shown in Fig. 6, high-magnification TEM images of all samples are taken near a depth range of 700 to 1000 nm for investigating the evolution of helium bubbles, which can be used to quantify the size and density of bubbles and evaluate the effect of annealing time on the behavior of helium bubbles. The specific statistical results are presented in Table 2 and Fig. 7; the TEM results reveal that as the annealing time prolonged, the size of bubbles increases and the density of bubbles decreases.

After annealed at 700 °C to 10 h, the helium bubble sizes increase from 1.12 nm to 1.67 nm and from 1 nm to 2.12 nm in the rolled and LPBF sample. It is evident that the helium bubbles remain relatively stable after a short soaking time of 10 h in both samples. The size of the helium bubbles in the LPBF sample was slightly larger than that of the rolled sample, but continued to grow in a stable range of helium bubble sizes [38], which had a minimal impact on helium embrittlement. A declining density of helium bubbles occurred in the two states of the samples. The helium bubble density in the LPBF sample was one order of magnitude lower than that in the rolled samples.

After annealing for 100 h, the helium bubble size in the rolled sample increases from 1.67 nm to 11.18 nm while in the LPBF sample from 2.12 nm to 8.5 nm. Significant coarsening of helium bubbles indicated a fast growth of helium bubbles in the 10–100-h annealing stage. The average size of helium bubbles in the two materials (rolled and LPBF samples) with the lowest and highest dislocation structure densities [20] was coarsened by 6.69 and 4.01 times, respectively. The density decreases from 1.84×10^{24} m^{-3} to 1.03×10^{23} m^{-3} in rolled sample and from 1.22×10^{23} m^{-3} to 7.76×10^{22} m^{-3} in LPBF sample with the decrease rate calculated as 94.4%, and 36.4%. Considering the bubble size and density evolution with annealing time, the helium bubbles in the LPBF samples grew steadily after the PIA treatment.

After 300 h of annealing, as shown in Fig. 7, the size and density of the helium bubbles have essentially reached a stable state for both samples, showing no significant alterations. Throughout the annealing process, the helium bubble density and the sensitivity of helium bubble coarsening to annealing time in the LPBF samples were lower than those of the rolled samples, indicating the excellent resistance of the LPBF samples to helium bubble growth.

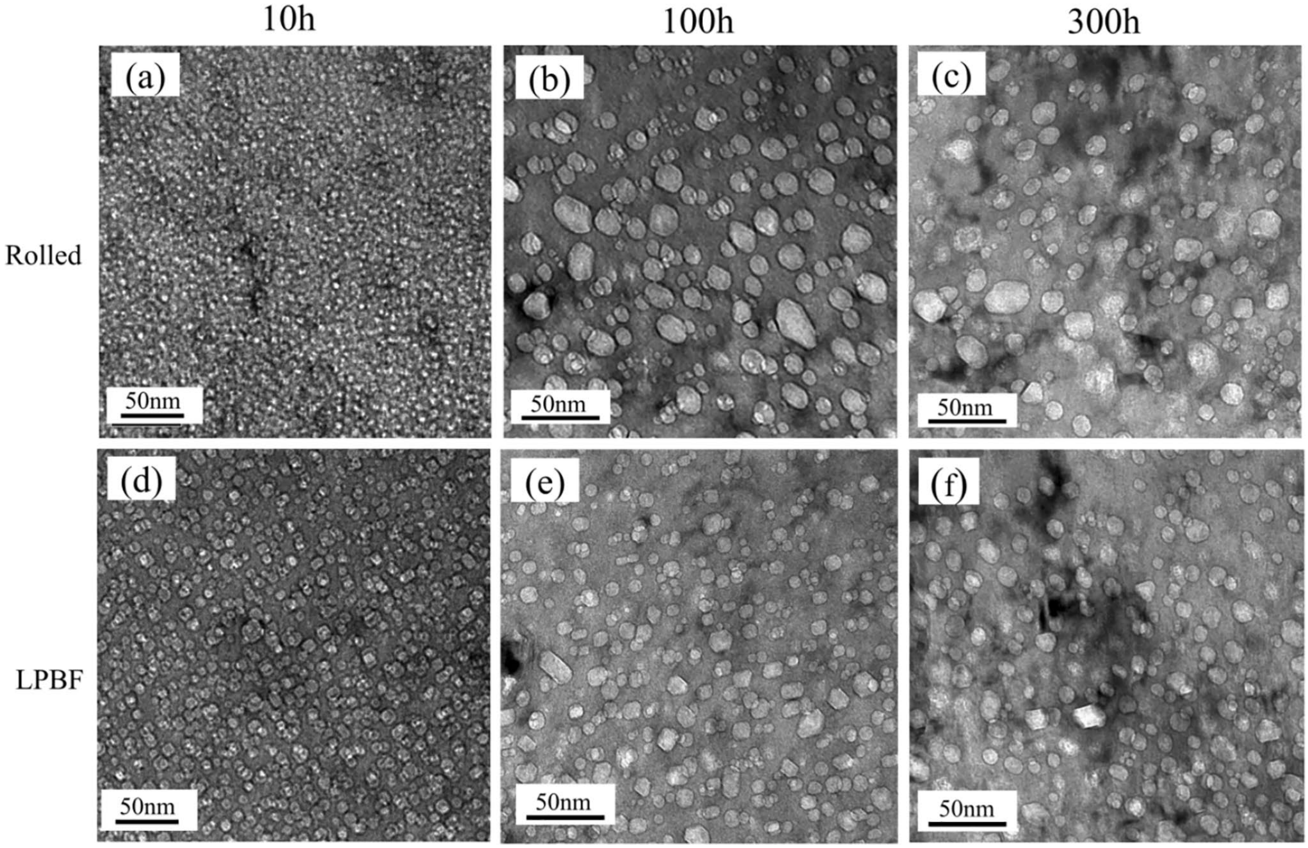

Fig. 6 TEM images of bubbles in post-irradiation annealed the rolled sample and the LPBF sample at 700 °C 10 h (**a**, **d**) and 100 h (**b**, **e**) and 300 h (**c**, **f**) in −500 nm under-focus condition

Table 2 Statistical results of the average size and quantity density of helium bubbles in rolled and LPBF samples as a function of annealing time

Label	Sample status	Average size of helium bubbles (nm)	Helium bubble density $\left(m^{-3}\right)$
T1	Rolled, implanted	1.12	3.86×10^{24}
T2	Rolled, implanted, PIA at 700 °C for 10 h	1.67	1.84×10^{24}
T3	Rolled, implanted, PIA at 700 °C for 100 h	11.18	1.03×10^{23}
T4	Rolled, implanted, PIA at 700 °C for 300 h	11.6	9.12×10^{22}
A1	LPBF, implanted	1.00	1.12×10^{24}
A2	LPBF, implanted, PIA at 700 °C for 10 h	2.12	1.22×10^{23}
A3	LPBF, implanted, PIA at 700 °C for 100 h	8.5	7.76×10^{22}
A4	LPBF, implanted, PIA at 700 °C for 300 h	8.93	6.73×10^{22}

3.3 Helium bubbles on nanoparticles

It is well known that the microstructure affects the behavior of helium bubbles in materials. To elucidate the diversity of the helium bubbles coarsening with increasing annealing time between LPBF and rolled 304L stainless steel, more detailed statistics of helium bubbles combined with the intrinsic structures are needed to assess the influence of the matrix microstructure. Figure 8 presents the evolution of the helium bubble nearby the nano-oxide particles in the LPBF samples. It can be observed that there is no significant accumulation of helium bubbles at the oxide-matrix interface without annealing. But a small number of helium bubbles are found to aggregate at the nano-oxide particles after annealing at 700 °C for 10 to 100 h, as indicated by the white arrows in Fig. 8b, c. However, almost no accumulation of helium bubbles was

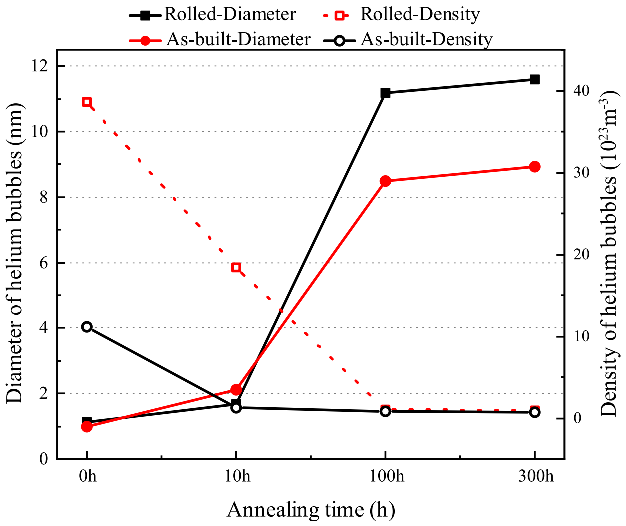

Fig. 7 Schematic diagram of the average diameter and number density of helium bubbles in the irradiated rolled sample and LPBF sample as a function of annealing time

observed at the oxide–matrix interface through the entire field of view after 300-h PIAed sample in Fig. 8d–f.

The results indicate that the nano-oxide–matrix interface is a defective sink for trapping helium atoms. The nanoparticles still possess sufficient trapping ability for helium bubbles even under long-term annealing, which can inhibit the dissociation or migration of helium bubbles. As shown in Fig. 8b, c, helium bubbles tended to preferentially aggregate at oxide particles relative to grain boundaries, which was consistent with Liu's research [39]. Molecular dynamics simulations can be employed to investigate the migration potential energy of helium bubbles toward grain boundaries and nano-oxide particles. It is speculated that the migration potential energy of helium bubbles toward nano-oxide particles might be lower, but further research is needed to delve into the mechanisms governing the evolution of helium bubbles in the presence of nano-oxide particles. This will contribute to reducing helium embrittlement and lay a solid theoretical foundation in the field of helium irradiation resistance.

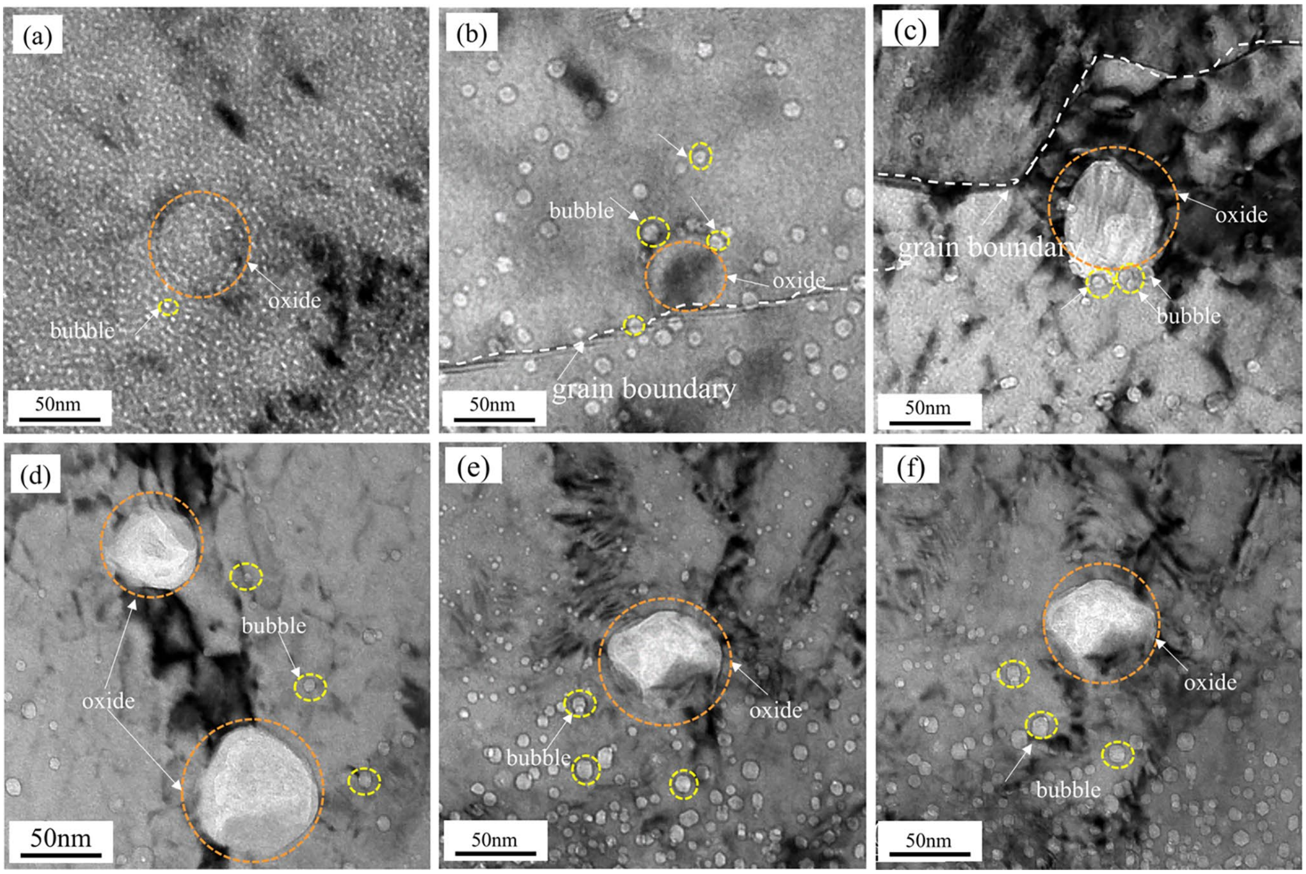

Fig. 8 Distribution of helium bubbles at nano-oxide particles in LPBF samples **a** unannealed; **b**, **c**, **d**–**f** annealed at 700 °C for 10, 100, 300 h, respectively

3.4 Helium bubbles on grain boundaries and dislocations

Figure 9 illustrates that within the annealing duration of 10 to 300 h, 96% of helium bubbles are distributed in proximity to dislocation structures, signifying a significant influence of these structures on the bubble growth process. In Fig. 9a, d, helium bubbles are notably aggregated along dislocation lines and complex dislocation structures. This observation suggests that complex dislocation structures exhibit strong adsorption and constraining effects on the helium bubbles. The micrograph shows that the helium bubbles on the dislocations are larger than those within the grains. This indicates that dislocations act as strong sinks and rapid diffusion paths for helium, causing bubbles to diffuse into shallow layers [26]. The bubble size and relative frequency of helium bubbles aggregating at the dislocations were counted and are depicted in Fig. 10. There was no significant difference in the size and frequency of helium bubbles between the LPBF and rolled samples for the 10-h PIAed samples. In the 100-h PIAed samples, however, an obvious helium bubble coarsening is occurred in the rolled sample with the bubble size ranging from 10 nm to 11.5 nm but from 8 nm to 10 nm in the LPBF sample. The proportion of large-size bubbles in the rolled sample was noticeably higher, with the maximum size even reaching 15 nm compared to the LPBF sample. With the annealing time extended to 300 h, the growth and evolution of helium bubbles tended toward stability in both the rolled and LPBF samples, with the bubble size and density remaining basically unchanged and the bubble size distribution remarkably similar, as shown in Figs. 7 and 10. The average bubble size is 10 to 12 nm for 300 h, compared to 10–11.5 nm for 100 h in rolled samples, and 8 to 10 nm for 100 h, compared to the 8.5–10.5nm for 300 h in LPBF samples. In contrast, most of the cellular subgrains were decomposed in the LPBF sample after 300 h of annealing, but many dislocations were still retained.

It is well known that the aggregation of helium bubbles at grain boundaries can cause intergranular cracking, which seriously affects the mechanical properties of materials. Therefore, it is essential to study the evolution behavior of helium bubbles at the grain boundaries. As shown in Fig. 11, helium bubbles are notably concentrated and distributed along grain boundaries with a larger size than those nearby the boundaries in both the rolled and LPBF samples. The bubble size increased with annealing time. This observation suggests that grain

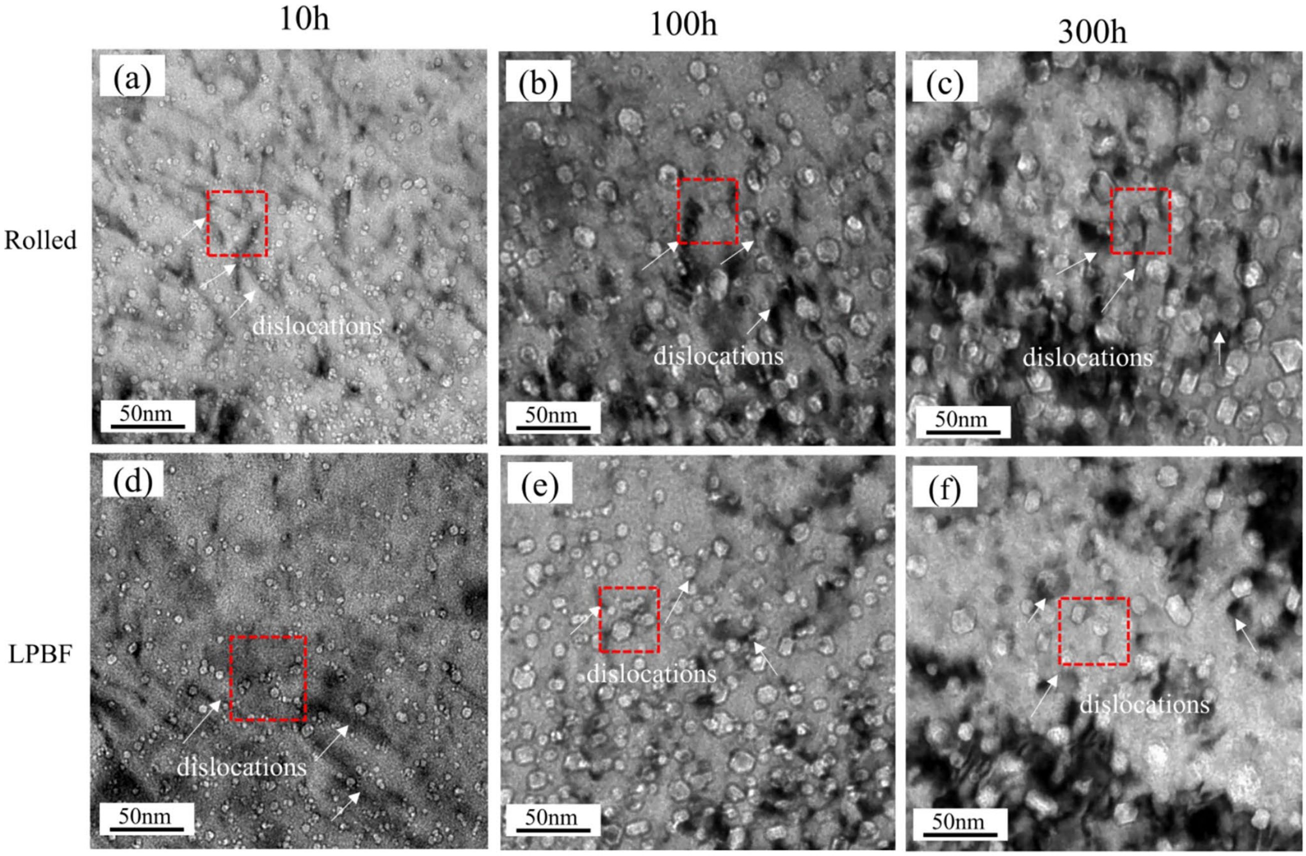

Fig. 9 Distribution of helium bubbles at dislocations in post-irradiation annealed the rolled sample and the LPBF sample at 700 °C 10 h (**a**, **d**) and 100 h (**b**, **e**) and 300 h (**c**, **f**)

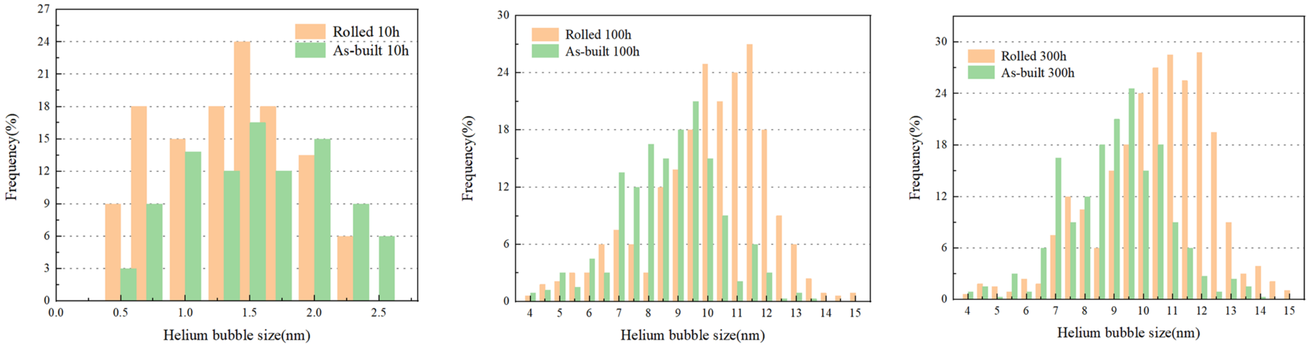

Fig. 10 Size and relative frequency of helium bubbles at dislocations in rolled and LPBF (as-built) samples at different annealing times

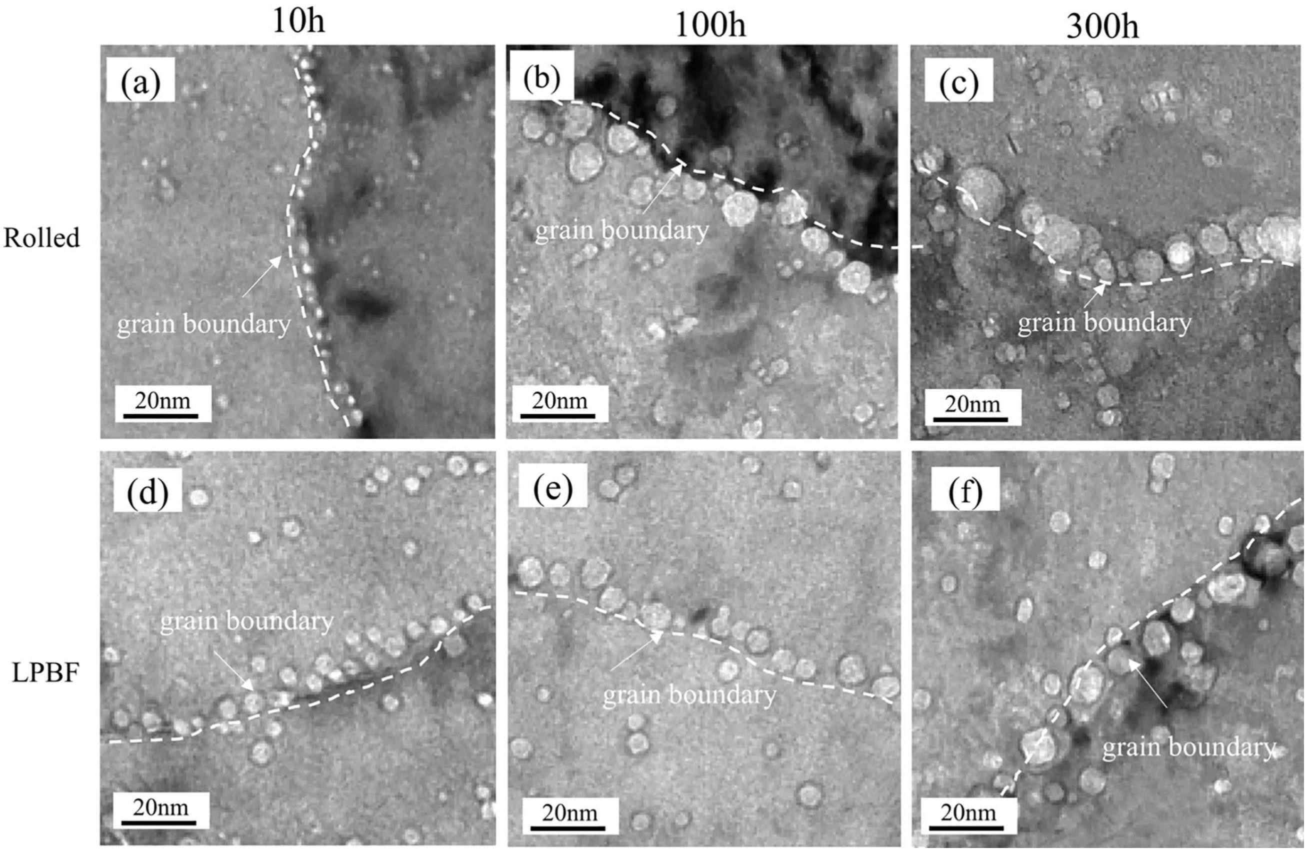

Fig. 11 Distribution of helium bubbles at grain boundaries in post-irradiation annealed the rolled sample and the LPBF sample at 700 °C 10 h (**a**, **d**), 100 h (**b**, **e**), and 300 h (**c**, **f**)

boundaries serve as effective sinks for point defects, facilitating the rapid nucleation and growth of helium bubbles at grain boundaries. The size distribution of the bubbles at the grain boundaries was statistically counted and is shown in Fig. 12. The LPBF samples exhibited restrained bubble coarsening with smaller helium bubble sizes than the rolled samples, indicating excellent resistance to helium irradiation. El-Atwani et al. [40] proposed that different orientations of grains can affect the size and density of helium bubbles. Helium bubbles are more likely to aggregate and grow along the [110] direction [41]. However, because multiple grains were not observed in this study, a detailed discussion on this aspect was not pursued.

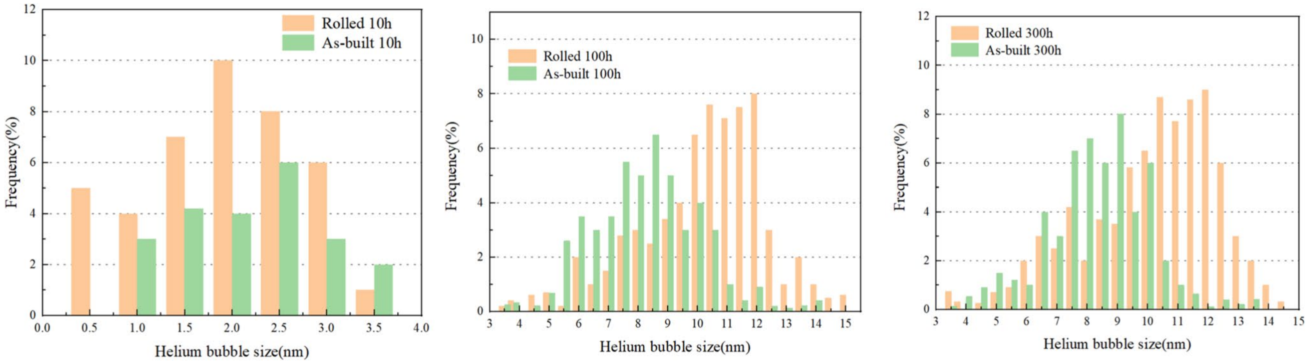

Fig. 12 Size and relative frequency of helium bubbles at grain boundaries in rolled and LPBF (as-built) samples at different annealing times

4 Discussion

4.1 Dependence of helium bubble evolution on annealing time

After annealing at 700 °C for 10,100, and 300 h, the bubble sizes of the irradiated samples follow the order A1 < T1 < T2 < A2 < A3 < A4 < T3 < T4 , showing slight discrepancies compared to previous research findings [32]. To investigate the underlying reasons, we simulated the curve of the density of helium bubbles with the reciprocal of the annealing temperature, conforming to Arrhenius law. The apparent activation energy $\left(E^{\text{act}}\right)$ was obtained from the slope of the corresponding curve, as shown in Fig. 13. The activation energies in the rolled and LPBF samples were calculated to be 0.42 and 0.29 eV, respectively. Previous research on the evolution of helium bubbles in metallic materials has confirmed that the activation energy of vacancy migration $\left(E_{\text{V}}^{\text{M}}\right)$ and the dissociation energy of He-vacancy (E^{diss}) are important parameters for selecting suitable helium diffusion modes. At the constant helium conditions, the following relations are obtained [42], where $E_{C_{\text{b}}}^{\text{act}}$ and $E_{R_{\text{b}}}^{\text{act}}$ are the apparent activation energies for helium bubble density and helium bubble diameter, respectively.

Vacancy mechanism:

$$E_{C_{\text{b}}}^{\text{act}} = -3E_{\text{V}}^{\text{M}}/14, E_{R_{\text{b}}}^{\text{act}} = E_{\text{V}}^{\text{M}}/14 \tag{1}$$

Replacement mechanism:

$$E_{C_{\text{b}}}^{\text{act}} = -3E_{\text{V}}^{\text{M}}/7, E_{R_{\text{b}}}^{\text{act}} = E_{\text{V}}^{\text{M}}/7 \tag{2}$$

Dissociative mechanism:

$$E_{C_{\text{b}}}^{\text{act}} = -E^{\text{diss}}, E_{R_{\text{b}}}^{\text{act}} = E^{\text{diss}}/3 \tag{3}$$

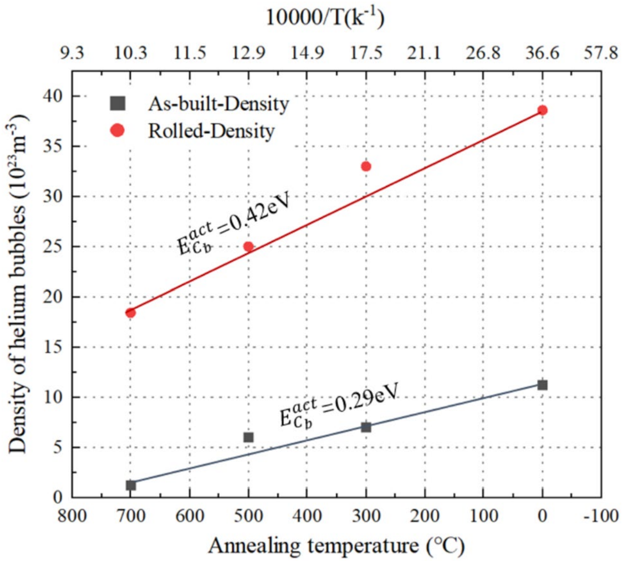

Fig. 13 Approximate simulation of the dependence of helium bubble density on annealing temperature in the helium concentration peak region of rolled and LPBF (as-built) samples annealed at 700 °C for 10 h

At low temperatures, the activation energy corresponding to the displacement mechanism is 0.43–0.56 eV [42, 43], and the vacancy migration energy is 1.0–1.3 eV [22, 44, 45]. At high temperatures, the dissociation energy corresponding to helium is approximately 3.0 eV [46]. In this study, helium atoms tended to diffuse more through the displacement mechanism.

The stability of helium bubbles is affected not only by the diffusion of helium atoms but also by the overall aggregation and coarsening of the bubbles [4, 47]. It is well known that migration and coalescence (MC) and Ostwald ripening (OR) are the two main coarsening mechanisms during the growth of helium bubbles, with different pressures within the bubble triggering different coarsening mechanisms. The Carnahan-Starling hard sphere equation of state provides a good approximation [48]:

$$\frac{P}{\rho kT} = \frac{\left(1 + y + y^2 - y^3\right)}{(1 - y)^3} \tag{4}$$

$$y = \frac{\pi \times \rho \times d^3}{6} \tag{5}$$

$$d = 0.3135\left[0.8542 - 0.03996 \ln\left(\frac{T}{9.16}\right)\right] \tag{6}$$

$$\frac{n}{n + 8.48 \times 10^{22}} = 4.3\% \tag{7}$$

$$n \times V_{\text{sample}} = \frac{4}{3} \times \pi \times r^3 \times \rho \times N \tag{8}$$

where k is the Boltzmann constant $\left(1.38 \times 10^{-23}\ \text{J/K/atom}\right)$, ρ is the helium atomic density in a bubble (atoms/nm^3), T is the temperature (K), and d is the hard sphere diameter of the helium atoms (nm). In this study, ρ was calculated assuming that the helium atoms in the helium bubbles were in equilibrium with the implanted helium atoms. The value of d was determined using the modified Buckingham potential. In the A2 sample ($T = 973\,\text{K}$), the calculation yields $d = 0.21$ nm and the mean helium concentration in the depth range of 700 nm − 900 nm was about 4.30 at.% based on SRIM results. The target density was 8.48×10^{22} atoms/cm^3, n is the number density of helium atoms in the region of peak helium concentration in units of atoms/nm^3. The value of n obtained from Eq. (7) was 3.65. Assuming that all the injected helium atoms are absorbed by the helium bubbles, Eq. (8) can be obtained, where V sample is the volume of the sample ($V_{\text{Sample}} = 250 \times 250 \times 52$), r is the mean radius of the helium bubble, N is the number of helium bubbles ($N = 1643$). The number density of helium atoms in the helium bubble was calculated using Eq. (7), and Eq. (8) was 1378 atoms/nm^3; the calculated internal pressure was approximately 23.35 GPa, which was significantly higher than the thermodynamic equilibrium equation of state value of 5.4 GPa [32]. These calculations indicate that overpressure helium bubbles suppress the occurrence of the OR mechanism and make helium bubbles more prone to coarsening through the MC mechanism [49, 50].

Based on the above analysis, it is speculated that the samples within 10 h of annealing have not yet reached the thermal equilibrium state. Therefore, helium atoms tend to diffuse more through the displacement mechanism, where the lattice position of He atoms is occupied by self-interstitial atoms (SIA) and transitions to the interstitial position. The migration and coalescence of the helium bubbles occurred. As the higher sink strength in the LPBF sample reduces vacancy supersaturation, the high-density dislocations in the LPBF samples act as the primary source of He atoms during annealing [51]. The re-release of helium atoms results in more helium bubbles migrating and aggregating in the form of helium atom clusters, and smaller He clusters exhibit higher mobility [52], resulting in a slightly larger helium bubble size in the LPBF sample than in the rolled sample. The specific mechanism is illustrated in Fig. 14.

4.2 Effect of intrinsic structure on the evolution of helium bubbles in LPBF 304L SS

It is well known that the existence of various defect structures in material systems can affect the evolution of helium

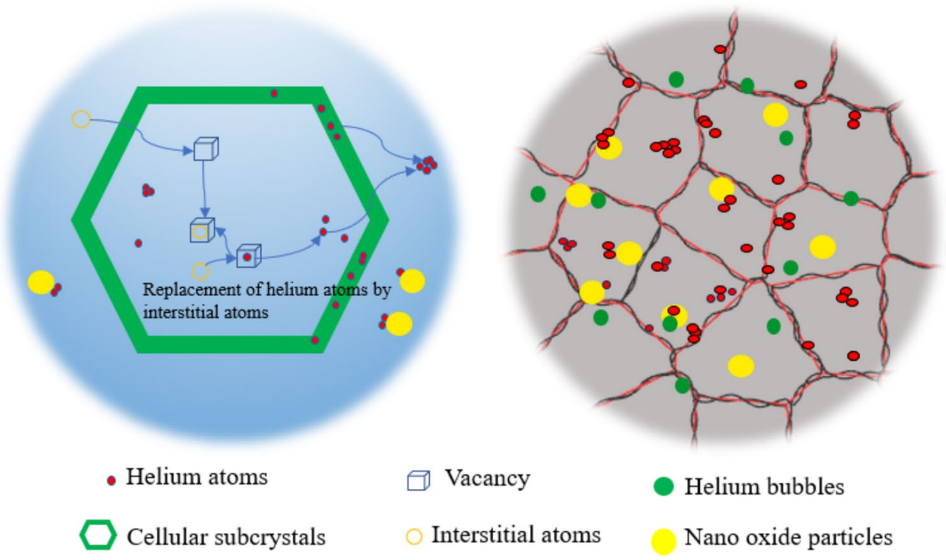

Fig. 14 Evolution mechanism diagram of helium bubbles in LPBF samples at 10-h annealing

bubbles. During annealing for 10–100 h, the helium bubbles aggregated at the oxide particle–matrix interfaces in the matrix (Fig. 8). This underscores their efficacy in restraining the growth of helium bubbles as sinks for point defects. Although this effect diminished after 300 h of annealing, it effectively inhibited the migration and coalescence of helium bubbles during their nucleation and rapid growth in the early stages. In contrast, helium bubbles exhibited strong aggregation and dense distribution at the cellular subgrain boundaries composed of dislocations throughout the matrix (Fig. 9), indicating the effective capture of helium bubbles by dislocations. The fundamental reason is that helium atoms tend to diffuse to dislocations with lower potential energies for nucleation and growth [12]. Regarding bubble growth during annealing, the dislocation lines serve as primary sources for vacancies, which have a strong affinity for helium atoms, making them more likely to aggregate and partially confined to the dislocation mesh [51]. The high-density dislocations in the LPBF samples were more effective in dispersing helium into smaller bubbles (Fig. 10), whereas in the rolled sample, the absence of high-density dislocations leaded to more pronounced coarsening of helium bubble sizes at dislocations. It was confirmed that high-density dislocations have a strong adsorption and confinement effect on helium bubbles and remain relatively stable even after 300 h of annealing.

The same results of helium bubble aggregation were also obtained at the grain boundaries (GB) (Fig. 11). The helium bubbles in the GBs of the LPBF sample were significantly smaller than those in the rolled sample. The bubbles at the grain boundaries in the rolled samples coarsened and exhibited a pronounced tendency to aggregate. This indicates that there are no strong defect sinks in the rolled sample to inhibit the growth of helium bubbles, and the nucleation of helium bubbles along the grain boundaries is likely to be assisted by enhancing the diffusion of helium along the grain boundaries, which occurs at lower activation energies [52, 53]. After 100 h of annealing, larger helium vacancy complexes became movable and were captured by grain boundaries, resulting in the net growth of helium bubbles [31, 54].

In contrast, LPBF 304L stainless steel has an abundance of interfaces, such as the high dislocation density around the cellular subgrains and the nano-oxide-matrix interface (Fig. 15) serve as capture sites for point defects. During the helium atom diffusion stage, these interfaces significantly enhanced the recombination of vacancies and interstitials. The depletion of vacancies inhibits the binding of vacancies and helium atoms and prevents the formation of helium bubbles [55, 56]. Regarding the nucleation stage of helium bubbles, these interfaces provide numerous nucleation sites for helium bubbles, which effectively disperse the aggregation of helium bubbles at grain boundaries and keep helium bubbles below the critical size for the bubble-to-cavity transition. Thus, the occurrence of helium embrittlement is reduced [50]. For the helium bubble growth stage under annealing, the high density of dislocations in the LPBF sample impedes the migration and merging of helium bubbles, inhibiting the overall coarsening of helium bubbles (Fig. 6) [57, 58].

It can be concluded that the high density of dislocations and nano-oxide particles in the LPBF sample can effectively mitigate radiation hardening and high-temperature He embrittlement, thereby extending the working time of structural materials in nuclear energy systems.

4.3 Swelling caused by helium bubbles

To compare the dependence of the swelling rate on annealing time, the swelling degree in the peak damage area was calculated for the LPBF and rolled samples, as shown in Fig. 16 [59]. When the annealing time was increased to 10 h, the material swelling rate was very weak with the extension of annealing time, and the two states of the samples exhibited almost identical material swelling. The rapid expansion of material swelling occurred in the period from 10 h to 100 h, especially the sharply increased swelling rate for the rolled sample but moderately for the LPBF samples because of the high density of dislocations. At the 100-h annealing time, the swelling rates of the rolled and LPBF samples were 3.2% and 1.47%, respectively. In LPBF samples, the presence of low-density and small helium bubbles reduces the overall swelling value [19]. This indicates that high-density dislocations are effective sinks for restricting the coarsening of helium bubbles by limiting their migration and aggregation of helium bubbles.

The capture effect of nano-oxide particles on helium bubbles was relatively weak compared to dislocation walls in LPBF 304L stainless steel, representing only a small amount of helium bubbles captured by the nano-oxide particle interfaces, along with the very small number of nano-oxide particles through the LPBF 304L stainless steel (Fig. 16). Therefore, it can be concluded that the dislocation structure in LPBF plays a major role in inhibiting the migration and growth of helium bubbles, and the sink strengths of dislocations (2.4×10^{14} m^{-2}) are approximately one order of magnitude higher than that of nano-oxide particles (2.1×10^{13} m^{-2}) [20]. Moreover, the stability of the dislocation structure surpasses that of nanoscale oxide particles after prolonged high-temperature annealing. This indicates that the high-density dislocations in the LPBF samples exhibit superior resistance to radiation-induced swelling compared with nanoscale oxide particles.

Fig. 15 Schematic diagram of the evolution of the helium bubble at 100 h of annealing: **a** LPBF sample, **c** rolled sample (**b** and **d** show enlarged schematic diagrams of **a** and **c**)

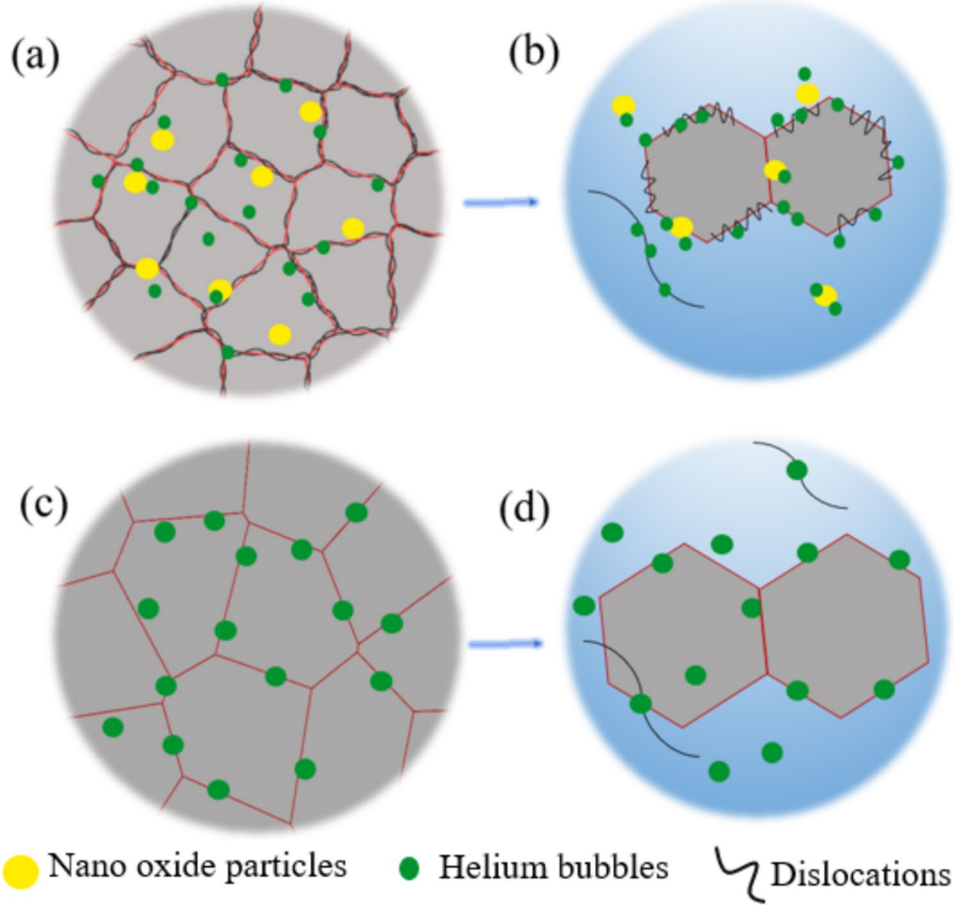

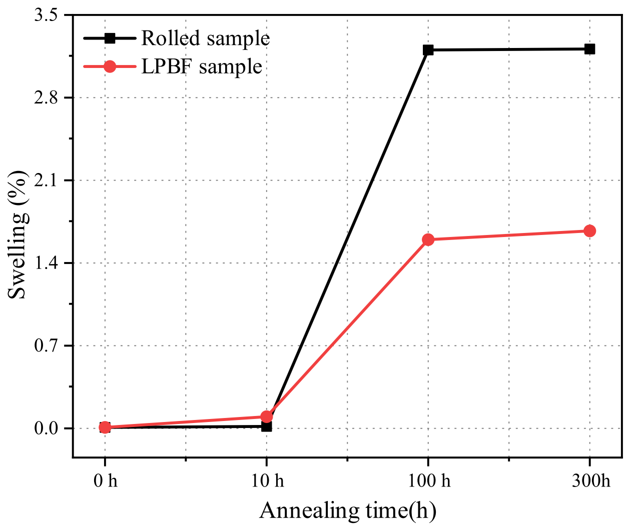

Fig. 16 Variation of swelling rate of rolled and LPBF (as-built) samples in the helium concentration peak region with annealing time

5 Conclusion

In this study, helium ion irradiation experiments were conducted at room temperature and annealed at 700 °C for 10, 100, and 300 h, respectively, to investigate the growth behavior of helium bubbles in LPBF 304L compared with conventionally rolled counterpart. The main conclusions are as follows:

1. Nucleation behavior of helium bubbles in LPBF: The depth of the helium bubble damage zone in LPBF samples is approximately 950 nm, the width is approximately 430 nm, and the density of helium bubbles in the peak helium concentration zone is 1.12×10^{24} m^{-3}. The depth of the helium-induced damage zone in the rolled samples is about 980 nm, the width is about 470 nm, and the density of helium bubbles in the peak helium concentration zone is 3.86×10^{24} m^{-3}. TEM revealed that the nanoprecipitates and high-density dislocations in LPBF can act as defect sinks to trap and annihilate point defects, and the LPBF samples have narrower irradiation damage regions and lower helium bubble densi-

ties. Therefore, LPBF samples have superior resistance to helium bubble nucleation.

2. Helium bubble growth behavior and swelling behavior of LPBF samples: The size of helium bubbles in rolled and LPBF samples increases and the density decreases with annealing time. After annealing for 10 h, the helium bubble size in LPBF samples is slightly larger than in rolled samples, which is due to the fact that the irradiated samples are in a state of disequilibrium. The surface activation energy (E^{act}) was calculated using by the Arrhenius model, which determined that helium atoms tend to diffuse through the substitution mechanism, and helium bubbles grow under the migration and coalescence (MC) mechanism. Annealing for 10–100 h is the period of rapid growth of helium bubbles, and after annealing for 100–300 h the bubbles enter a period of stable growth. Compared with the rolled samples, the LPBF samples have lower swelling coefficients after the post-irradiation annealing treatment, so it can be speculated that the LPBF samples have excellent resistance to helium bubble coarsening.
3. Microstructure of LPBF samples: During the annealing period of 10–100 h, the cellular subgrains and the oxide nanoparticles of the material remain stable and have a strong trapping effect on helium bubbles, and after annealing for 300 h, the cellular subgrains begin to decompose and the oxide nanoparticles no longer provide trapping for helium bubbles, which indicates that the oxide nanoparticles are not as stable as high-density dislocations, and at this time, the high-density dislocations become the main factor inhibiting helium bubble growth in LPBF samples. The LPBF samples still have excellent resistance to helium irradiation in a long-term service environment.

Author Contributions All authors contributed to the study conception and design. Material preparation, data collection, and analysis were performed by Si-Yi Qiu, Yan-Lin Gu, and Yu-Yu Guo. The first draft of the manuscript was written by Si-Yi Qiu, and all authors commented on previous versions of the manuscript. All authors read and approved the final manuscript.

Data Availability The data that support the findings of this study are openly available in Science Data Bank at https://cstr.cn/31253.11.sciencedb.j00186.00752 and https://doi.org/10.57760/sciencedb.j00186.00752.

Declarations

Conflict of interest The authors declare that they have no conflict of interest.

References

1. Q.B. Nguyen, Z. Zhu, F.L. Ng et al., High mechanical strengths and ductility of stainless steel 304L fabricated using selective laser melting. J. Mater. Sci. Technol. **35**, 388 (2019). https://doi.org/10.1016/J.JMST.2018.10.013
2. A.T. Sutton, C.S. Kriewall, M.C. Leu et al., Characterization of laser spatter and condensate generated during the selective laser melting of 304L stainless steel powder. Addit. Manuf. **31**, 100904 (2020). https://doi.org/10.1016/j.addma.2019.100904
3. A. Pardo, M.C. Merino, A.E. Coy et al., Influence of Ti, C and N concentration on the intergranular corrosion behaviour of AISI 316Ti and 321 stainless steels. Acta Mater. **55**, 2239 (2007). https://doi.org/10.1016/J.ACTAMAT.2006.11.021
4. H. Trinkaus, B.N. Singh, Helium accumulation in metals during irradiation—Where do we stand? J. Nucl. Mater. **323**, 229 (2003). https://doi.org/10.1016/j.jnucmat.2003.09.001
5. S.H. Li, J.T. Li, W.Z. Han, Radiation-induced helium bubbles in metals. Materials (Basel). **12**, 1036 (2019)
6. S.R. Soria, A. Tolley, E.A. Sánchez, The influence of microstructure on blistering and bubble formation by He ion irradiation in Al alloys. J. Nucl. Mater. **467**, 357 (2015). https://doi.org/10.1016/j.jnucmat.2015.09.051
7. K. Yutani, H. Kishimoto, R. Kasada et al., Evaluation of Helium effects on swelling behavior of oxide dispersion strengthened ferritic steels under ion irradiation. J. Nucl. Mater. **367–370**, 423 (2007). https://doi.org/10.1016/J.JNUCMAT.2007.03.016
8. G.M. Bond, D.J. Mazey, M.B. Lewis, Helium-bubble formation and void swelling in nimonic PE16 alloy under dual-ion (He^+, Ni^+) irradiation. Nucl. Instrum. Methods Phys. Res. **209–210**, 381 (1983). https://doi.org/10.1016/0167-5087(83)90827-X
9. S. Nogami, A. Hasegawa, T. Tanno et al., High-temperature helium embrittlement of 316FR steel. J. Nucl. Sci. Technol. **48**, 130 (2011). https://doi.org/10.3327/jnst.48.130
10. H. Ullmaier, Helium in fusion materials: high temperature embrittlement. J. Nucl. Mater. **133–134**, 100 (1985). https://doi.org/10.1016/0022-3115(85)90118-7
11. F. Micheli, Methylphenylethynylpyridine (MPEP) Novartis. Curr. Opin. Investig. Drugs **1**, 355 (2000)
12. S.J. Zinkle, L.L. Snead, Designing radiation resistance in materials for fusion energy. Annu. Rev. Mater. Res. **44**, 241 (2014). https://doi.org/10.1146/annurev-matsci-070813-113627
13. R. Schäublin, A. Ramar, N. Baluc et al., Microstructural development under irradiation in European ODS ferritic/martensitic steels. J. Nucl. Mater. **351**, 247 (2006). https://doi.org/10.1016/J.JNUCMAT.2006.02.005
14. L. Kurpaska, I. Jozwik, M. Lewandowska et al., The effect of Ar-ion irradiation on nanomechanical and structural properties of ODS RAF steels manufactured by using HIP technique. Vacuum **145**, 144 (2017). https://doi.org/10.1016/J.VACUUM.2017.08.039
15. Z. Sun, Y. Xu, F. Chen et al., Effects of ion irradiation on microstructure of 316L stainless steel strengthened by disperse nano TiC through selective laser melting. Mater. Charact. **180**, 111420 (2021). https://doi.org/10.1016/j.matchar.2021.111420
16. X. Sun, F. Chen, H. Huang et al., Effects of interfaces on the helium bubble formation and radiation hardening of an austenitic stainless steel achieved by additive manufacturing. Appl. Surf. Sci. **467–468**, 1134 (2019). https://doi.org/10.1016/j.apsusc.2018.10.268
17. D. Xu, F. Chen, X. Tang et al., Effect of LaB_6 addition on mechanical properties and irradiation resistance of 316L stainless steels processed by selective laser melting. Int. J. Adv. Nucl. React. Des. Technol. **3**, 74 (2021). https://doi.org/10.1016/j.jandt.2021.06.004
18. J. Hou, W. Chen, Z. Chen et al., Microstructure, tensile properties and mechanical anisotropy of selective laser melted 304L stainless

steel. J. Mater. Sci. Technol. **48**, 63 (2020). https://doi.org/10.1016/J.JMST.2020.01.011
19. C. Fu, J. Li, J. Bai et al., Effect of helium bubbles on irradiation hardening of additive manufacturing 316L stainless steel under high temperature He ions irradiation. J. Nucl. Mater. (2021). https://doi.org/10.1016/j.jnucmat.2021.152948
20. J. Hou, B. Dai, Y. Li et al., Helium bubble nucleation in Laser Powder Bed Fusion processed 304L stainless steel. J. Nucl. Mater. **542**, 152443 (2020). https://doi.org/10.1016/j.jnucmat.2020.152443
21. L. Wang, X.P. Wang, L.F. Zhang et al., Helium desorption behavior and growth mechanism of helium bubbles in FeCrNi film. Nucl. Mater. Energy (2019). https://doi.org/10.1016/j.nme.2019.100710
22. C.H. Zhang, K.Q. Chen, Y.S. Wang et al., Temperature dependence of bubble structure in 316L stainless steel irradiated with 2.5 MeV He ions. J. Nucl. Mater. **258–263**, 1623 (1998). https://doi.org/10.1016/S0022-3115(98)00332-8
23. Y.R. Lin, W.Y. Chen, L. Tan et al., Bubble formation in helium-implanted nanostructured ferritic alloys at elevated temperatures. Acta Mater. (2021). https://doi.org/10.1016/j.actamat.2021.117165
24. C. Fu, J. Li, J. Bai et al., Evolution of helium bubbles in SLM 316L stainless steel irradiated with helium ions at different temperatures. J. Nucl. Mater. (2022). https://doi.org/10.1016/j.jnucmat.2022.153609
25. I. Villacampa, J.C. Chen, P. Spätig et al., Helium bubble evolution and hardening in 316L by post-implantation annealing. J. Nucl. Mater. **500**, 389 (2018). https://doi.org/10.1016/j.jnucmat.2018.01.017
26. J. Chen, S. Romanzetti, W.F. Sommer et al., Helium bubble formation in 800 MeV proton-irradiated 304L stainless steel and alloy 718 during post-irradiation annealing. J. Nucl. Mater. **304**, 1 (2002). https://doi.org/10.1016/S0022-3115(02)00874-7
27. Q. Li, C.M. Parish, K.A. Powers et al., Helium solubility and bubble formation in a nanostructured ferritic alloy. J. Nucl. Mater. **445**, 165 (2014). https://doi.org/10.1016/j.jnucmat.2013.10.048
28. Y. Chen, Y. Li, G. Ran et al., In-situ TEM observation of microstructure evolution in $Fe_9Cr_1{\cdot}5W_0{\cdot}4Si$ alloy during He^+ irradiation and post-implantation annealing. J. Nucl. Mater. **555**, 153126 (2021). https://doi.org/10.1016/j.jnucmat.2021.153126
29. W.B. Liu, Y.Z. Ji, P.K. Tan et al., Microstructure evolution during helium irradiation and post-irradiation annealing in a nanostructured reduced activation steel. J. Nucl. Mater. **479**, 323 (2016). https://doi.org/10.1016/j.jnucmat.2016.07.030
30. F. Carsughi, H. Ullmaier, H. Trinkaus et al., Helium bubbles in FeNiCr after post-implantation annealing. J. Nucl. Mater. **212–215**, 336 (1994). https://doi.org/10.1016/0022-3115(94)90082-5
31. P.D. Edmondson, C.M. Parish, Q. Li et al., Thermal stability of nanoscale helium bubbles in a 14YWT nanostructured ferritic alloy. J. Nucl. Mater. **445**, 84 (2014). https://doi.org/10.1016/j.jnucmat.2013.10.024
32. H. Liu, S. Min, M. Jiang et al., Helium bubble growth in He^+ ions implanted 304L stainless steel processed by laser powder bed fusion during post-irradiation annealing at 600 °C. Acta Metall. Sin. (English Lett.) **35**, 1509 (2022). https://doi.org/10.1007/s40195-022-01391-w
33. H. Liu, S. Min, M. Jiang et al., Helium bubble nucleation in laser powder bed fusion processed 304L stainless steel. J. Nucl. Mater. **542**, 152443 (2020). https://doi.org/10.1016/j.jnucmat.2020.152443
34. J.F. Ziegler, M.D. Ziegler, J.P. Biersack, SRIM—the stopping and range of ions in matter (2010). Nucl. Instrum. Methods Phys. Res. Sect. B Beam Interact. Mater. Atoms. **268**, 1818–1823 (2010). https://doi.org/10.1016/j.nimb.2010.02.091
35. H. Liu, S. Min, M. Jiang et al., Helium bubble growth in He^+ ions implanted 304L stainless steel processed by laser powder bed fusion during post-irradiation annealing at 600 °C. Acta Metall. Sin. (English Lett.) **35**, 1509 (2022). https://doi.org/10.1007/s40195-022-01391-w
36. C.H. Hung, Y. Li, A. Sutton et al., Aluminum parts fabricated by laser-foil-printing additive manufacturing: processing, microstructure, and mechanical properties. Materials (Basel) (2020). https://doi.org/10.3390/ma13020414
37. R. Li, B. Fu, Y. Wang et al., Effect of cold-rolling reduction on recrystallization microstructure, texture and corrosion properties of the X2CrNi12 ferritic stainless steel. Materials (Basel) (2022). https://doi.org/10.3390/ma15196914
38. G.R. Odette, D.T. Hoelzer, Irradiation-tolerant nanostructured ferritic alloys: transforming helium from a liability to an asset. JOM **62**, 84 (2010). https://doi.org/10.1007/s11837-010-0144-1
39. H. Liu, J. Huang, C. Wang et al., Effects of grain boundaries and nano-precipitates on helium bubble behaviors in lanthanum-doped nanocrystalline steel. Scr. Mater. **200**, 113900 (2021). https://doi.org/10.1016/J.SCRIPTAMAT.2021.113900
40. O. El-Atwani, J.E. Nathaniel, A.C. Leff et al., The role of grain size in He bubble formation: implications for swelling resistance. J. Nucl. Mater. **484**, 236 (2017). https://doi.org/10.1016/j.jnucmat.2016.12.003
41. M. Miyamoto, H. Takaoka, K. Ono et al., Crystal orientation dependence of surface modification in molybdenum mirror irradiated with helium ions. J. Nucl. Mater. **455**, 297 (2014). https://doi.org/10.1016/j.jnucmat.2014.06.030
42. V. Zell, H. Schroeder, H. Trinkaus, Helium bubble formation in nickel during hot implantation. J. Nucl. Mater. **212–215**, 358 (1994). https://doi.org/10.1016/0022-3115(94)90086-8
43. S. Jublot-Leclerc, M.L. Lescoat, F. Fortuna et al., TEM study of the nucleation of bubbles induced by He implantation in 316L industrial austenitic stainless steel. J. Nucl. Mater. **466**, 646 (2015). https://doi.org/10.1016/j.jnucmat.2015.09.013
44. K. Nakata, S. Takamura, I. Masaoka, Electrical resistivity recovery in Fe-Cr-Ni alloys after neutron irradiation at low temperature. J. Nucl. Mater. **131**, 53 (1985). https://doi.org/10.1016/0022-3115(85)90424-6
45. A. De Backer, G. Adjanor, C. Domain et al., Modeling of helium bubble nucleation and growth in austenitic stainless steels using an Object Kinetic Monte Carlo method. Nucl. Instrum. Methods Phys. Res. Sect. B **352**, 107 (2015). https://doi.org/10.1016/j.nimb.2014.11.110
46. J. Rothaut, H. Schroeder, H. Ullmaier, The growth of helium bubbles in stainless steel at high temperatures. Philos. Mag. A Phys. Condens. Matter. Struct. Defects Mech. Prop. **47**, 781 (1983). https://doi.org/10.1080/01418618308245265
47. B.N. Singh, H. Trinkaus, An analysis of the bubble formation behaviour under different experimental conditions. J. Nucl. Mater. **186**, 153 (1992). https://doi.org/10.1016/0022-3115(92)90330-N
48. R.E. Stoller, G.R. Odette, Analytical solutions for helium bubble and critical radius parameters using a hard sphere equation of state. J. Nucl. Mater. **131**, 118 (1985). https://doi.org/10.1016/0022-3115(85)90450-7
49. V.N. Chernikov, H. Trinkaus, H. Ullmaier, Helium bubbles in nickel annealed at $T >$ 0.7 Tm. J. Nucl. Mater. **250**, 103 (1997). https://doi.org/10.1016/S0022-3115(97)00275-4
50. H. Trinkaus, The effect of internal pressure on the coarsening of inert gas bubbles in metals. Scr. Metall. **23**, 1773 (1989). https://doi.org/10.1016/0036-9748(89)90359-1
51. J. Liu, H. Huang, A. Liu et al., The effects of post-irradiation isochronous annealing on defects evolution and hardening in Hastelloy N alloy. J. Nucl. Mater. **548**, 152855 (2021). https://doi.org/10.1016/j.jnucmat.2021.152855

52. Z. Yan, T. Yang, Y. Lin et al., Effects of temperature on helium bubble behaviour in Fe–9Cr alloy. J. Nucl. Mater. **532**, 152045 (2020). https://doi.org/10.1016/j.jnucmat.2020.152045
53. C. Herzig, Y. Mishin, Grain boundary diffusion in metals. In *Diffusion in Condensed Matter*, ed. by P. Heitjans, J. Kärger (Springer, Berlin, Heidelberg, 2005), pp. 337–366. https://doi.org/10.1007/3-540-30970-5_8
54. P.L. Lane, P.J. Goodhew, Helium bubble nucleation at grain boundaries. Philos. Mag. A Phys. Condens. Matter Struct. Defects Mech. Prop. **48**, 965 (1983). https://doi.org/10.1080/01418618308244330
55. X.M. Bai, A.F. Voter, R.G. Hoagland et al., Efficient annealing of radiation damage near grain boundaries via interstitial emission. Science **327**, 1631 (2010). https://doi.org/10.1126/science.1183723
56. G. Ackland, Controlling radiation damage. Science **327**, 1587 (2010). https://doi.org/10.1126/science.1188088
57. P.D. Edmondson, C.M. Parish, Y. Zhang et al., Helium bubble distributions in a nanostructured ferritic alloy. J. Nucl. Mater. **434**, 210 (2013). https://doi.org/10.1016/j.jnucmat.2012.11.049
58. K.Y. Yu, Y. Liu, C. Sun et al., Radiation damage in helium ion irradiated nanocrystalline Fe. J. Nucl. Mater. **425**, 140 (2012). https://doi.org/10.1016/j.jnucmat.2011.10.052
59. T. Yang, C. Lu, K. Jin et al., The effect of injected interstitials on void formation in self-ion irradiated nickel containing concentrated solid solution alloys. J. Nucl. Mater. **488**, 328 (2017). https://doi.org/10.1016/j.jnucmat.2017.02.026